RSC Advances

PAPER

View Article Online
View Journal | View Issue



Cite this: *RSC Adv.*, 2016, **6**, 17460

# $Al_2O_3$ micro- and nanostructures affect vascular cell response

Karin Kiefer,†‡[a] Gürler Akpınar,†[b] Ayman Haidar,[a] Tuba Ikier,[c] Cağrı Kaan Akkan,§[d] Erhan Akman,[c] Juseok Lee,[d] Marina Martinez Miró,[d] Elif Kaçar,[c] Arif Demir,[c] Michael Veith,[e] Dilek Ural,[f] Murat Kasap,*[bg] Mehmet Kesmez,[h] Hashim Abdul-Khaliq[a] and Cenk Aktas¶‖*[d]

Received 18th October 2015
Accepted 1st February 2016

DOI: 10.1039/c5ra21775j

www.rsc.org/advances

In-stent restenosis (ISR) is one of the most common and serious complications observed after stent implantation. ISR is characterized by the inordinate proliferation of smooth muscle cells (SMC) that leads to narrowing of the blood vessels. To achieve a healthy endothelium, it is critical to selectively enhance the growth of endothelial cells (EC) while suppressing the growth of smooth muscle cells, which is still a major challenge and yet to be achieved. In this study, novel surfaces have been developed to support the selective growth of endothelial cells. Micro- and nanostructured $Al_2O_3$ surfaces with unique topographical features were fabricated and tested. Surface characterization and cellular response of endothelial cells (HUVEC) as well as smooth muscle cells (HUVSMC) has been investigated at cellular and molecular levels. A topography driven selective cell response of ECs over SMCs was demonstrated successfully. This selective response of ECs was also analyzed at protein levels in order to understand the basic mechanism.



## 1. Introduction

In-stent restenosis (ISR), which is a common and serious problem observed after stent implantation, may lead to fatal complications.[1] ISR is characterized by the excessive proliferation of smooth muscle cells (SMC) that leads to the narrowing of the vascular lumen.[2] Various methods have been developed to reduce the proliferation of SMC using specific anti-proliferative drugs such as taxol, statins, angiopeptin and *etc.*[3] On the other hand, such drugs also lead to a delay in the formation of a healthy endothelial layer.[4] It is still a major challenge to control the competition between SMC and endothelial cell (EC) proliferation and coverage on the substratum. The cell–substratum interaction is governed by a number of physical and chemical characteristics of the substrate. It has been shown that the surface topography plays a major role especially at early stages of the endothelialization.[5] Blanchemain *et al.* showed that EC and SMC exhibit diverse responses to the surface topography.[6] While SMC proliferation decreased about 60% on plasma-chemical process modified non-woven membranes, EC proliferation was reduced about only 10% on the same topographic features. This study and other similar research strongly indicate that surface topography may act as an effective tool for blocking of excessive SMC proliferation and enhancing the adhesion and growth of EC simultaneously.

As the use of nanostructured materials is increasing in different applications, there are various studies that highlight how drastically these new materials may enhance bio-interfacial interactions, including protein adsorption and subsequent cellular responses.[7] We have demonstrated that 1D nanostructures deposited on glass substrates induce selective adhesion and proliferation of ECs in comparison to SMCs in one of our previous study.[8] Similarly, Mohan *et al.* showed that nanostructured titanium samples led to a significant enhancement in the cellular viability and proliferation of EC and a subsequent decrease in SMC proliferation in comparison to unmodified flat

[a]*Clinic for Paediatric Cardiology, Saarland University, 66421 Homburg, Germany*
[b]*DEKART Proteomics Laboratory, Medical School, Kocaeli University, Umuttepe, 41380 Kocaeli, Turkey. E-mail: mkasap2008@gmail.com*
[c]*Laser Technology Research and Application Center, Kocaeli University, Yenikoy, Basiskele, 41380 Kocaeli, Turkey*
[d]*INM—Leibniz Institute for New Materials, 66123 Saarbrücken, Germany. E-mail: oca@tf.uni-kiel.de*
[e]*Department of Inorganic Chemistry, Saarland University, 66123 Saarbrücken, Germany*
[f]*Department of Cardiology, Medical School, Kocaeli University, Umuttepe, 41380 Kocaeli, Turkey*
[g]*Department of Medical Biology, Medical School, Kocaeli University, Umuttepe, 41380 Kocaeli, Turkey*
[h]*Research and Development Center, Meliksah University, 38280 Kayseri, Turkey*
† These authors contributed equally to this work.
‡ Current address: INM—Leibniz Institute for New Materials, 66123 Saarbrücken, Germany.
§ Current address: Boğaziçi University Institute of Biomedical Engineering, Biomaterials, Kandilli Kampüs, Istanbul, Turkey.
¶ Current addresses: (a) Chair for Multicomponent Materials, Institute for Materials Science, Christian Albrechts University of Kiel, 24118 Kiel, Germany.
‖ (b) Research and Development Center, Meliksah University, 38280 Kayseri, Turkey.

titanium samples.[9] It is also known that microtopography of the substratum greatly influences cellular responses such as adhesion, proliferation and differentiation.[10]

In terms of topography extra cellular matrix (ECM) is a heterogeneous mixture of structures which have different sizes and shapes.[11] Although ECM is composed of nanoscaled structures, the combination and organization of these form a microscale and even a mesoscale topography.[12] Especially cardiac and cardiovascular tissue has a complex architecture that covers a wide spectrum of length scales ranging from the nano- to the microscale.[13] In this context *in vitro* studies on multi-scale topography may lead to a more realistic model for cell–substratum studies in the field of cardiac implants.

In our previous study we showed that multi-scaled surface features (micro- and nano-scaled structures) enhanced the endothelialisation process.[14] We structured the surface of the stainless steel substrate with short laser pulses in order to obtain unique topographical features. The ablation from the surface led to formation of micro-craters (with a diameter of around 50 μm) and much finer nanostructures (50–100 nm) around them. When the interspacing between micro-craters was kept around 75–150 μm, we observed a clear reduction in the myofibroblast (MF) population (which are indicators of α-SMA-expressing cells which contribute to accelerated restenosis[15]) without disturbing the proliferation of EC.

In this current work, we compared the interaction of Human Umbilical Vein Endothelial Cells (HUVEC) and Human Umbilical Vein Smooth Muscle Cells (HUVSMC) on nanostructured and micro-/nanostructured surfaces. Here, we introduced a novel approach for the fabrication of nanostructured and micro-/nanostructured surfaces which exhibit improved selectivity for endothelialisation process. While chemical vapour deposition (CVD) was employed to fabricate nanostructured surface properties, the laser treatment was used to create a secondary microtopography (micro-/nanostructured surface). We used standard glass slides as the model substrate due to its proven biocompatibility and ease of use for especially optical characterization. The core–shell (metal–metal oxide: aluminium–aluminium oxide) nature of deposited nanostructures led, by its intrinsic chemical meta-stability, to a complete oxidation upon laser treatment. Obtaining an identical surface composition ($Al_2O_3$) on topographic features deposited on glass ensures a reliable comparison between different topographies that is only the result of topography effect. The cellular interactions of HUVEC and HUVSMC with the substrates were proven and the biocompatibility was determined. Furthermore, to evaluate the changes that may occur at the molecular level on these surfaces, a proteome analysis study was carried out with HUVEC cells. The results of the proteome study indicated the presence of changes in cellular architecture.

## 2. Results and discussion

### 2.1 Morphology and surface characterization

We aimed the synthesis of surfaces with unique topographical features by combing CVD and laser surface treatment. Our "molecule-to-material" approach based on the decomposition of the molecular precursor leads to a nanostructured surface. The decomposition of the molecular precursor $(^tBuOAlH_2)_2$ at elevated temperature (550–600 °C) yields a nanostructured surface composed of 1D $Al_2O_3$ nanostructures on glass substrate. Such a typical topography is visualized schematically in Fig. 1A. Following the laser treatment micro-craters were obtained on formerly deposited nanostructured layer as the secondary topography (schematically shown in Fig. 1B). One can see that the morphology of the inner surface of such a micro-crater looks obviously different than the topography features observed on as-deposited (not laser treated) layers (Fig. 1D and E). SEM image in Fig. 1C shows the morphology of deposited 1D $Al_2O_3$ nanostructures in detail. The chaotic morphology composed of tangled and crossing high aspect-ratio (AR) nanostructures reminds of a spaghetti-like structure. In contrast to the state of the art vapour liquid solid (VLS) approach, such 1D nanostructures grew without using any additional catalysis particle on the substrate surface. Since it is a catalyst free synthesis one can deposit such nanostructures on any metal or metal-oxide surface, too. In this context, identical structures (layers deposited on the glass substrate) can be easily fabricated on the surface of metallic implants. On the other hand such a catalyst free synthesis led to a random growth rather than aligned 1D nanostructures that are mostly observed in a typical VLS process.[16]

Irradiation of the surface by a short laser pulse induced micro-craters with a diameter of 45–50 μm on the surface. Average depth of these micro-craters was measured to be around 100 nm deep. High-energy laser pulse leads to a sudden increase in the surface temperature. It seems that the ablation occurs as a consequence of possible ultra-fast melting and evaporation (accompanied with a high re-coil pressure) taking place at elevated surface temperature. It can be stated that while a crater like morphology forms after the ejection of material from the surface, the fast-solidification after the short laser pulse leads to a porous secondary microtopography within this micro-crater (as shown in Fig. 1E). High surface tension during the ultra-fast heating/cooling cycle and the intense re-coil pressure may be the main reasons of such a porous morphology formation

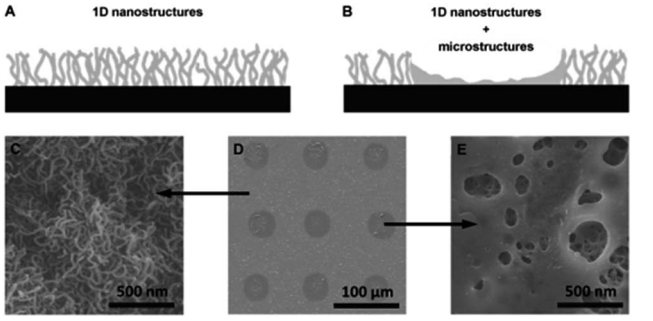


Fig. 1 Schematic presentation of (A) as deposited layer (nanostructured surface) and (B) laser treated layer (micro-/nanostructured surface). SEM images of (C) as deposited layer (nanostructured surface), (D) laser treated layer (micro-/nanostructured surface) and (E) inner surface of a micro-crater.

upon the solidification following the high heat transfer from the exothermic reaction of nano aluminium to alumina.

While the deposited 1D structures form a nano-topography on the surface, the laser treatment forms the micro-structuring step of our process. By combining both we achieved a micro-/nanostructured surface. Our previous study shows that the surface chemistry before and after the laser treatment stays identical.[17] The deposited nanostructures are in the form of core–shell (metal–metal oxide) morphology while the inner core is made of Al and the wrapping shell consists of $Al_2O_3$. During the excessive heating followed by the laser ablation, the Al-core contacts oxygen molecules in the vicinity, oxidizes completely and transform into $Al_2O_3$, which is a highly exothermic reaction (see Fig. 2A and C). Due to the ultra-short melting/solidification cycle and the high recoil pressure, newly forming $Al_2O_3$ layer within the micro-crater (formed after the ablation) exhibits a highly porous morphology with micro-cracks (Fig. 2B and D). The formation of such a discontinuous oxide layer seems to be related with the flow of the molten layer and its subsequent solidification over 1D nanostructures that were not subjected to high temperatures gradients due to limited heat dissipation through the deposited layer (as seen below the molten top layer in Fig. 2D). It can be stated that the thermal penetration depth is much shorter than the thickness of the deposited layer because of the short pulse duration (8–12 ns) and also the nanoporous structure of deposits.

With the help of a micro-lens array that is comprised of several lenses (separated with an interspacing of 150 μm in two axes) more than 4000 micro-craters (with a diameter of 40–50 μm) were obtained after a single laser pulse. By moving the whole substrate under the focused laser beam, a periodic pattern comprised of equally interspaced micro-craters (over a nanostructured surface) is achieved. One can alter the diameter of each micro-crater and the interspacing between them by simply changing the type of the micro-lens array. In this preliminary study we aimed synthesis of micro-craters with a diameter size of around 50 μm since we have previously shown that such microstructures do not disturb the EC proliferation.[14] In another study, we have shown that by combining micro-craters with an underlying nano-topography one can get extremely hydrophilic surfaces.[18] In this context, we applied a similar interspacing (around 150 μm) between the micro-craters to obtain a good wetting.

Our wetting analysis shows that both as-deposited and laser treated surface exhibit a hydrophilic nature. This is in accordance with our observations on plasma etched and laser structured poly ether ether ketone (PEEK) surfaces.[18] On the other hand, our micro-/nanostructured surface exhibits a long-lasting hydrophilic behaviour compared to surfaces that have solely nanostructured features and manufactured *via* plasma etching method. While similar nanostructures achieved by plasma etching of polymers exhibit a hydrophilic behaviour just after the etching process, the water contact angle increases gradually by time. This instability is mostly attributed to the change of the chemical state of the surface by time. We did not observe any significant change in wetting of both as-deposited (nanostructured) and laser treated (micro-/nanostructured) surfaces. Both surfaces exhibited a contact angle of around 10° and did not show any change in the contact angle (data is not shown), which clearly indicates a stable hydrophilic character (Fig. 3A). Roughness measurements (Fig. 3B) show that while the $R_a$ value is around 120 nm, it shows a slight increase to 135 nm after the laser treatment. Such an increase can be explained with newly induced crater like structures over the nanostructures which cover the whole surface. It can be stated that due to the ultra-short laser pulse (8–12 ns), the ablation from the surface was limited to some nanometers and therefore we did not observe a drastic change in the average roughness. This may be the reason of the similarity in the wetting characteristics of both surfaces since the surface chemistry stays identical. On the other hand, there is a clear difference in the morphology of the surface structures. While as-deposited layer is mainly composed of highly tangled and interpenetrated 1D nanostructures, laser treated surface is composed micro-craters (with a diameter of 40–50 μm) and 1D nanostructures between them. Within these micro-craters there are pores with diameters of 50–200 nm. It can be concluded that such surfaces are ideal to study the effect of the geometry and size of surface features on cellular responses regardless of their wetting angle and surface roughness (which are mostly given as main determinants affecting the cellular response to the substratum).

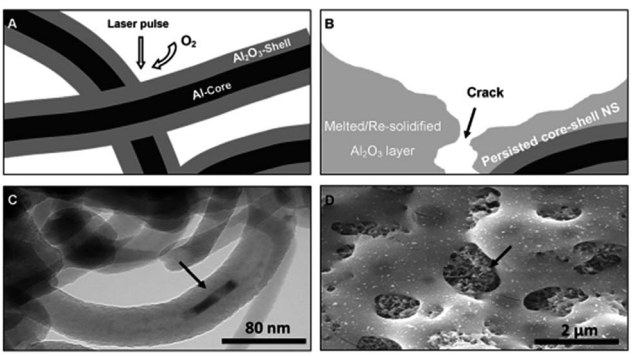


Fig. 2 (A) Schematic presentation of the laser assisted oxidation and transformation to $Al_2O_3$, (B) schematic presentation of the crack formation and melt flow/solidification $Al_2O_3$ layer, (C) TEM image of as-deposited 1D nanostructures with core–shell morphology (arrow shows core–shell structure) and (D) SEM image of deposited layer after the laser treatment (arrow shows the persisted nanostructures below the molten and re-solidified $Al_2O_3$ layer).

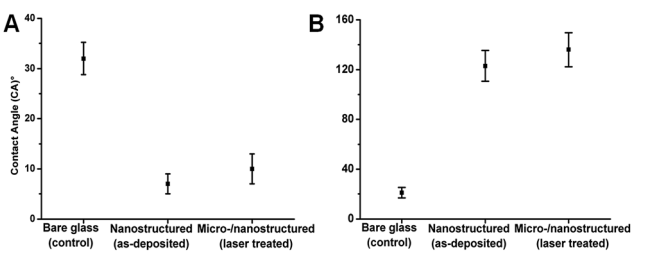


Fig. 3 (A) Contact angle and (B) roughness measurements of bare glass, nanostructured and micro-/nanostructured surfaces.

 

### 2.2 Determination of viability (WST-1 assay)

After the sample sterilization, biocompatibility and cell growth tests on modified surfaces have been carried out. Therefore HUVECs and HUVSMCs were seeded on the samples and cultivated up to 72 h. Afterwards a WST-1 assay was performed to determine the viability of each cell type on each surface owing different topographical features (Fig. 4). HUVECs showed the highest measured viabilities for all tested samples and incubation times (Fig. 4A). The measured viability decreased for all tested samples but stayed constant on this level of around 80% compared to control cells (Fig. 4A). A marginal better viability could be detected for the micro-/nanostructured surface. Alongside, the viability of HUVSMCs cultured on micro-/nanostructured surfaces was significantly reduced in comparison to control cells (Fig. 4B). After 24 h incubation SMCs possessed a viability of around 50% on nanostructured and 40% on micro-/nanostructured surfaces. With increasing cultivation time up to 72 h, the viability further decreased on nanostructured surface to 35% whereas it stayed constant for micro-/nanostructured surface (Fig. 4B). The obtained results clearly indicate that EC have a much higher viability on micro-/nanostructured surfaces than SMC. With increasing incubation times, especially the nanostructured surface led to a further viability reduction for SMC as they could not adapt onto these surfaces.

### 2.3 Cellular adhesion and morphology

After assessing the viability of the two used cell types on different surfaces, the cellular adhesion and morphology were investigated using immunohistochemical staining as well as scanning electron microscopy. For this, HUVEC and HUVSMC were cultivated on sterilized samples up to 72 h, fixed and stained with specific antibody (Fig. 5). The analysis of the immunohistochemical staining illustrated the morphology and cell growth of EC and SMC. HUVEC possessed their typical polygonal shape on the glass control (Fig. $5A_1$). The F-actin network could clearly be visualized and vinculin focal adhesions identified in the periphery. The adaptor protein vinculin is known to take part in cellular adhesion and mediates cell–matrix-interactions as well as motility. Here it plays a profound role.[19] After 24 h cultivation, attached endothelial cells started to proliferate. Alongside ECs grown on the structured surfaces possessed a similar but partly reduced cell size with less developed actin network but stronger vinculin signal in the periphery and also in the cytoplasm (Fig. $5A_2$ and $A_3$). With increasing the incubation time up to 72 h, HUVEC proliferated on all tested samples starting to form a layer. Again ECs on bare glass showed a well-developed filamentous actin network and distinct cell–substrate adhesion sites (Fig. $5B_1$). ECs on both structured surfaces showed an increased spreading and proliferation forming a cell layer. Again a higher vinculin signal could be detected for both cell–surface interactions (Fig. $5B_2$ and $B_3$).

Additionally the adhesion and morphology of SMCs were investigated. For both incubation times (24 and 72 h) we found best cellular adhesion, morphology and cell growth on bare glass (Fig. $5C_1$ and $D_1$). Here, the typical spindle like structure with a huge cell body and a centralized nucleus could be observed. SMCs on glass featured a well-developed F-actin network and strong cell–substrate adhesion sites that were mostly located in the periphery. In contrast, SMCs cultivated on the micro-/nanostructured surfaces were much smaller and less spread but possessed a high vinculin signal through the whole cell. Furthermore, only few cells sticking near to each other were detected (Fig. $5C_2$ and $C_3$). With increasing the incubation time, SMCs on both structured surfaces showed increased but still reduced attachment compared to cells on the control. Nevertheless the attached cells possessed an actin-signal through the whole cell and distinct focal adhesions on all tested surfaces (Fig. $5D_2$ and $D_3$). These findings are in accordance with the

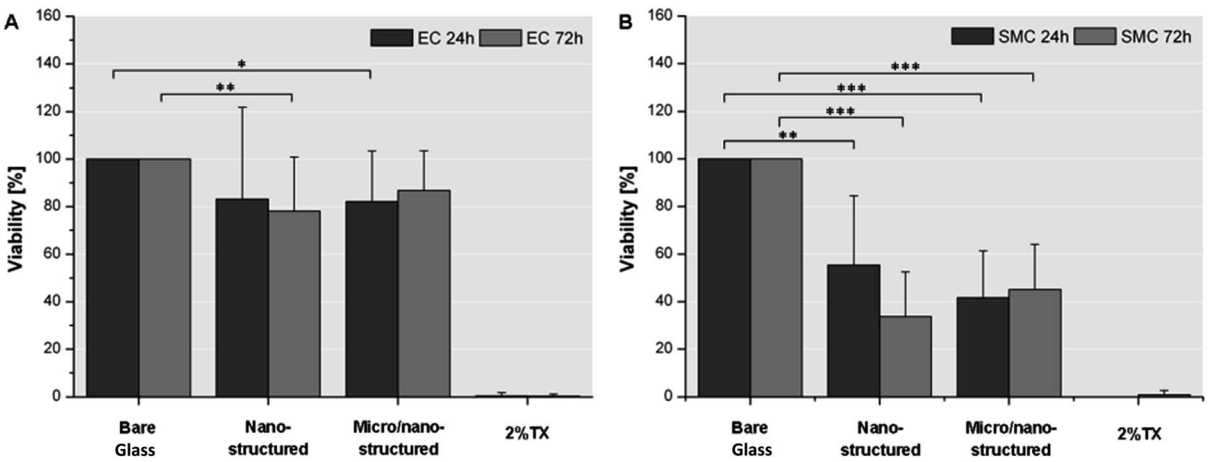


Fig. 4 Determination of cell viability (WST-1). HUVEC (A) and HUVSMC (B) were cultivated for 24 and 72 h on bare glass, nanostructured and micro-/nanostructured surfaces. Afterwards cell viability was measured using WST-1 assay. Each value displays the mean cellular viability ± standard deviation of seven independent experiments. Viability was determined as percentage of viable cells compared to the amount of viable cells grown on glass. 2% Triton X-100 treated cells (2% TX) were used as negative control. The differences in viability between cells grown on glass and those grown on structured surfaces were: significant when $P < 0.05$ (*), very significant when $P < 0.01$ (**) and extremely significant when $P < 0.001$ (***).

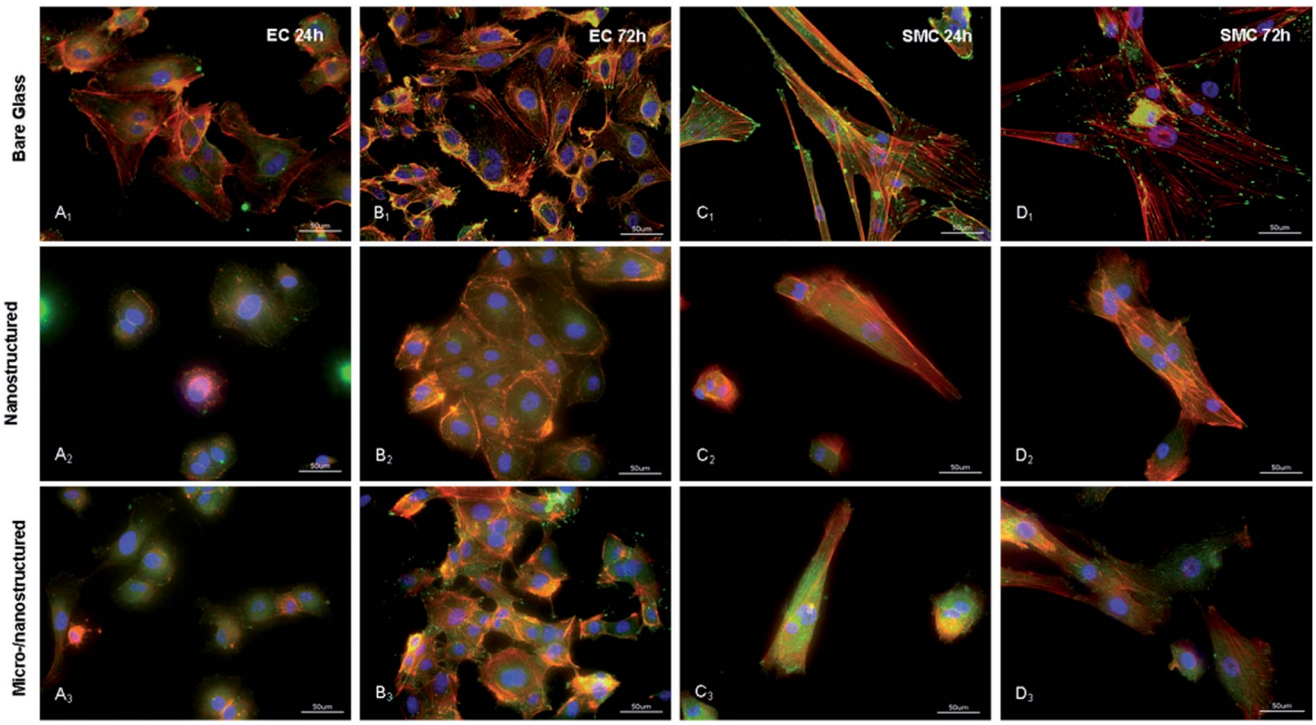


Fig. 5 Cellular morphology and focal adhesion. HUVEC (A & C) and HUVSMC (B & D) were cultivated for 24 and 72 h on the different structured surfaces (nanostructured; micro-/nanostructured) ($A_{1-3}$–$D_{1-3}$). Nuclei were visualized using DAPI (blue), F-actin using AlexaFluor555-conjugated phalloidin (red) and focal adhesion points using anti-vinculin antibody (AlexaFluor488-labeled goat-anti-rabbit secondary IgG antibody, green). Scale bars: 50 μm.

previously described results from viability assay. Again, SMC were only able to adhere weakly onto the nanostructured surfaces. Our results indicate that the underlying structures influenced the cellular adhesion of the different cell types. It has been demonstrated that an altered surface topography takes part in actin reorganization and cellular attachment over focal adhesions. Nikkhah *et al.* also suggested that microscale topographical cues can be used to precisely control adhesion, morphology and migration among others.[20] For further and more detailed information regarding the morphology of HUVECs and HUVSMCs respectively, scanning electron microscopy analysis was performed (Fig. 6). Through this analysis, the received staining results could be confirmed. ECs possessed again the strongest adhesion and cell growth especially on glass (Fig. $6A_1$).

ECs were characterized over their polygonal shape and SMCs were depicting as spindle like. Both cell types possessed a flat and well spread morphology with distinct filopodia and lamelopodia. The introduction of nano- as well as nano/microstructures led in both cell lines to a reduced cell size. After 24 h incubation, less ECs grew on the modified surfaces. With increasing incubation time, ECs started to form a layer. Initially ECs did not adhere completely to the substrate (Fig. $6A_3$), but with increasing incubation time the cell–surface contact increased.

According the results provided in the previous sections, it is conceivable that EC adapted to the underlying structures. On the other hand, SMCs were most likely not able to overcome hindrances in attachment (Fig. $6B_2$). Fewer cells, compared to probed controls could be detected. After both incubations times, SMCs could not attach themselves sufficiently to the surface and the morphology varied from control cells even after longer incubation time. These results indicate that SMCs were only weakly able to adhere onto the new surface and are in accordance with viability and immunohistochemical staining results. It can be concluded that underlying surface topography promoted a selective microenvironment and fostered especially the adhesion of endothelial cells.

In previous studies, it could be shown that cell–substratum interaction is influenced by topographical cues.[21] Also a selective cell response to surface topography in terms of adhesion, proliferation, or morphology has been discussed for different cell lines. It is well known that different cell types react in a different manner on different surface modifications. Plenty of research has been performed to analyse the influence of an underlying topography for a variety of surfaces and cell lines such as fibroblast,[17] myofibroblast,[14] neurons,[22] endothelial cells,[8] and cardiomyocytes.[23]

### 2.4 Protein analysis using MALDI TOF/TOF

After completing the measurements and analysis concerning cellular viability and morphology, changes on the proteome level were investigated. Compared with HUVECs, HUVSMCs failed to reach the adequate and necessary confluence on both

 

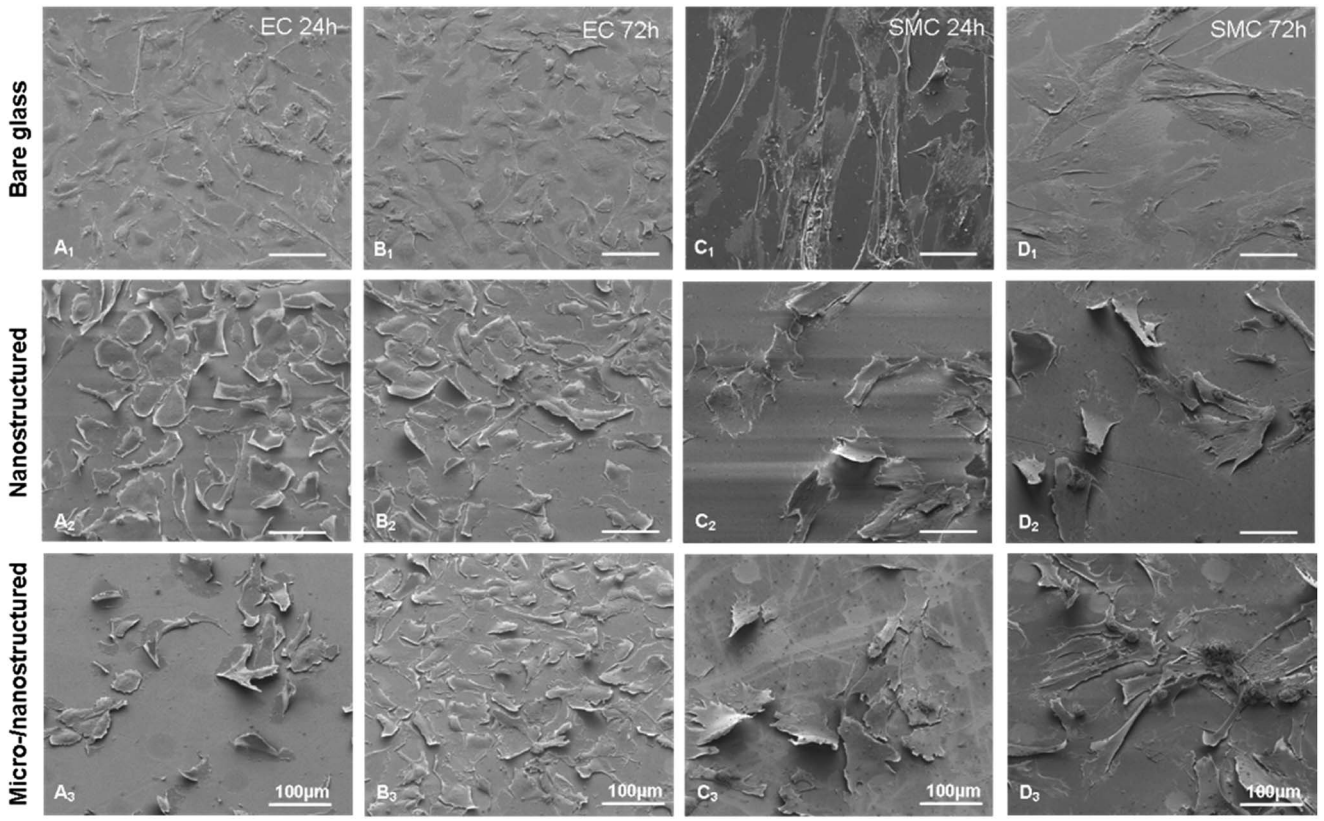


Fig. 6 Cellular adhesion and morphology. HUVEC (A & C) and HUVSMC (B & D) were cultivated for 24 and 72 h on the different structured surfaces (nanostructured; micro-/nanostructured). Afterwards SEM analysis was performed. Scale bar: 100 µm.

nanostructured surfaces. Therefore, proteome analysis could only carry out with HUVECs (Fig. 7).

After 2D-DIGE gel electrophoresis, gel images were taken and analysed with PDQuest Advance software. A total of 569 ± 5 spots were detected in each gel. 511 of these were matched to every member. There was a 99% match rate with a correlation coefficient of 0.943. When two-fold up/down regulation criteria was used, five proteins were noticeably up/down-regulated in cells growing on micro-/nanostructured surfaces (Table 1). These proteins were lamin A/C (LMNA), vimentin (VIME), tubulin alpha-1C chain (TUBA1C), keratin 8 (K2C8) and triosephosphate isomerase (TPI). All proteins except TBA1C were up-regulated in ECs cultured on nano-and microstructured surfaces. VIME and LMNA showed the highest protein values on nanostructured surfaces whereas TPI and K2C8 were dominantly expressed on nano-and microstructured surfaces. The down regulation of TBA1C was comparable for cells cultured on MNS surfaces. Getting a deeper view into the discovered proteins, we found that three proteins (LMNA, VIME, K2C8) were members of the intermediate filament (IF) family, one belonging to microtubules (TUBA1C) and the last one is part of glycolysis (TPI). IF and microtubules are major components of the cytoskeleton of eukaryotes and therefore responsible for mechanical strength.[24] Keratin belongs to types I and II – acidic and basic keratins. Predominantly keratins are expressed in the intracytoplasmic cytoskeleton of epithelial tissue but an expression in some human vascular endothelial cells of soft tissue could also be shown.[25] The second IF was lamin. LMNA was also found to be up regulated in ECs especially on nanostructures. LMNAs belong to the type V intermediate filament protein family and are responsible for the maintenance of the cell nucleus.[26] They fulfill different task like dissociation and reassembly of the nuclear membrane after mitosis, post mitotic

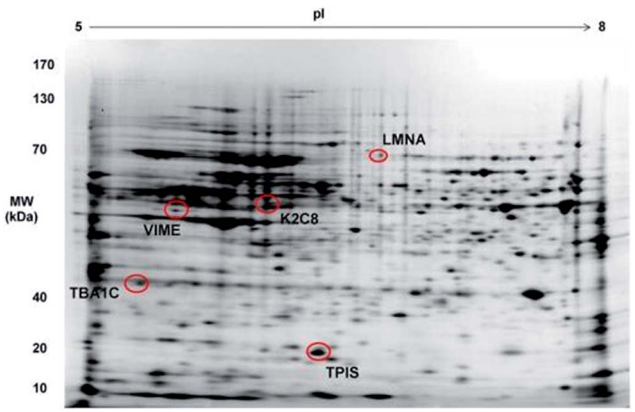


Fig. 7 2D gel of whole cell proteome of HUVECs. Equal amounts of protein have been subjected to isoelectric focusing on linear 11 cm pH 5–8 IG strips. Spots that were positively identified (Table 1) are marked by red circles. LMNA: laminin-A; VIME: vimentin; K2C8: keratin; TBA1C: tubulin alpha-1C chain; TPI: triosephosphate isomerase.

Table 1 MALDI MS/MS results for the five identified spots that were up or down regulated after cultivation on different structured surfaces compared with bare glass[a]

| Spot number | Accession number (Uniprot) | Protein name | MW (kDa) | MALDI (MS/MS) protein score | Regulation (up ↑ and down ↓) | Function |
|---|---|---|---|---|---|---|
| 4602 | P05787 | K2C8 | 53 671 | 249 | 3.49 fold ↑* | Intermediate filament |
| 6102 | P60174 | TPI | 26 653 | 212 | 2.45 fold ↑* | Enzyme |
| 2605 | P08670 | VIME | 53 619 | 272 | 5 fold ↑** | Intermediate filament |
| 4402 | P02545 | LMNA | 74 095 | 131 | 0.39 fold ↓*** | Intermediate filament |
| 2502 | Q9BQE3 | TUBA1C | 49 863 | 105 | 3 fold ↓ | Microtubules |

[a] * micro-/nanostructured surface *vs.* bare glass; **: nanostructured surface *vs.* bare glass; *** micro-/nanostructured surface *vs.* nanostructured surface.



reorganization, and anchoring of the nucleus within the cytoplasm.[27] The third IF, showing the highest up-regulation compared to glass, was vimentin (Fig. 8).

Here, cells cultured on nanostructured surfaces possessed a five time higher expression. VIME is a type III intermediate filament protein that is expressed in endothelial and other mesenchymal cells.[28] The highly conserved vimentin filaments undergo extensive reorganization upon phosphorylation to control disassembly and assembly[29] and interact with several proteins. Here, VIME modulates the integrin-mediated cell attachment. Gonzales *et al.*[30] described the structure and function of a vimentin-associated matrix adhesion (VMA) in endothelial cells. VMAs are composed, among others, of different components like vinculin, specific integrins, plectin, and vimentin. VMA in endothelial cells is assembled by actively migrating cells and promotes motility. Hence, the higher protein expression is in accordance with the immunohistochemical staining of vinculin (Fig. 5). Here especially on nanostructured surfaces, a stronger vinculin staining was detected. Interestingly, TPI was found to be up-regulated on MNS surfaces. This enzyme is responsible for the reversible interconversion of the triose phosphate isomers D-glyceraldehyde 3-phosphate and dihydroxyacetone phosphate. TPI is a major player in glycolysis and is necessary for efficient energy production.[31] Hence, the increased expression can be associated with an increased energy requirement.

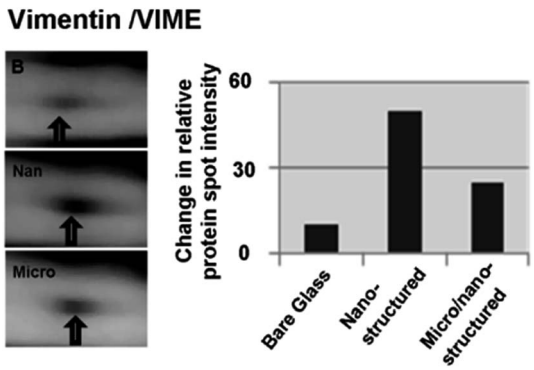


Fig. 8 Changes in relative vimentin protein spot intensity. Proteins were identified by MALDI-ToF mass spectroscopy in spots excised from 2D-DIGE gels of lysates from cells cultivated on bare glass (BG), nanostructured (nano) and micro-/nanostructured (micro) surfaces. The intensity of vimentin spots were defined and the changes in relative protein spot intensity determined.

# 3. Materials and methods

## 3.1 Deposition of nanostructures

1D $Al_2O_3$ (Al-core/$Al_2O_3$-shell) nanostructures were deposited on glass slides by CVD of the molecular precursor $(^tBuOAlH_2)_2$ as we have already explained in detail.[32] After cleaning with ethanol, the glass slides were fixed on the heating stage of the customized vertical cold-wall CVD chamber.[33] The molecular precursor $(^tBuOAlH_2)_2$ was fed into the chamber when the substrate temperature reached to 550 °C and the pressure of the chamber was reduced to $10^{-3}$ mbar with help of a rough pump. After a deposition period of 30 min, samples were subjected to cooling under the vacuum conditions.

## 3.2 Laser treatment

Deposited layers were structured using an nanosecond pulsed Nd:YAG laser (Continuum Surelite III) in air without any protective atmosphere. The laser was operated at 300 mW power, 10 Hz repetition rate and 532 nm wavelength which is the second harmonic generation. The laser beam was shaped using a Galilean type expander and sent to the sample surface through a lens array composed of several micro lenses (separated with an interspacing of 150 μm in two axes) to induce periodical structures on the substrate surface. Each micro lens has a diameter of 140 μm and a focal length of 6.7 mm.

## 3.3 Surface characterization

Scanning electron microscopy (SEM-JEOL-6400F) operating at an acceleration voltage of 15 kV was used to obtain a detailed morphological analysis of the prepared surfaces. Prior to SEM analysis samples were affixed on a conductive carbon tape, mounted on the support and sputtered with approximately 10 nm of thick layer of gold/palladium (40/60). Transmission electron microscopy (CM20 TEM Philips) was used to reveal the core–shell structure of deposited 1D nanostructures following a standard thinning step. A contact angle analysis system (Kruess G2, Hamburg, Germany) was used to determine the wetting characteristics of surfaces. Double distilled water ($^{dd}H_2O$ with a volume of 5 μl) was used as the test liquid and the average value of five measurements was defined as the contact

 

angle. Roughness analysis was carried using a mechanical profilometer (Zeiss Surfcom 1500 SD3, Gottingen, Germany) and the average roughness ($R_a$) was calculated from five different measurements at a scanning range of 10 μm.

### 3.4 Cell culture

For all experiments EC and SMC from the human umbilical vein (HUVEC, HUVSMC; PromoCell, Heidelberg, Germany) were used. HUVEC were cultured at 37 °C and 5% $CO_2$ in endothelial cell growth medium including supplements (C-22010, PromoCell) and HUVSMC accordingly in smooth muscle cell growth medium (C-22062, PromoCell). For all experiments, cleaned and sterilized samples (3 h, 180 °C) were transferred into sterile well plates. Then, cells were seeded with a density of 250 cells per $mm^2$ onto the substrates and cultivated for 24 and 72 h, respectively. Three different samples have been tested and the cellular response has been determined: $Al_2O_3$ nanostructured without (nanostructured surface) and with laser treatment (micro-/nanostructured surface), and bare glass slides as control.

### 3.5 Determination of cell viability (WST-1 assay)

WST-1 assay (Cell Proliferation Reagent; Roche Diagnostics, Mannheim, Germany) was used to determine the cellular viability. Accordingly, both cell lines were cultivated as described before (see Section 3.4). After each incubation time, the samples were transferred into new well plates and washed once with cell culture medium. Subsequently, WST-1 reagent was added and the formazan formation was measured as a sign of cell viability according to the instruction manual provided by the manufacturer. The mean absorbance of cells grown on glass was defined as 100%. Accordingly the absorbance of cells grown on the substrate was related to this value. 2% Triton X-100 treated cells were used as negative control. Statistical analysis was performed using the Student's *t*-test. The differences in viability between cells grown on glass and those grown on structured surfaces were: significant when $P < 0.05$ (*), very significant when $P < 0.01$ (**) and extremely significant when $P < 0.001$ (***).

### 3.6 Characterization of cellular adhesion

The cellular adhesion and attachment onto the different surfaces were visualized using immunohistochemical staining. HUVEC and HUVSMC were cultivated on the different samples as described before (see Section 3.4). Subsequently, the samples were washed, fixed using 4% PFA (paraformaldehyde; Sigma-Aldrich, Deisenheim, Germany) and permeabilized using 0.1% Triton X-100 solution (Carl Roth, Karlsruhe, Germany). After blocking with 1% BSA (bovine serum albumin; Sigma-Aldrich, Deisenheim, Germany) the primary antibody against vinculin (MAB357, Millipore) was added for 1 h. Then, all of the samples were incubated with fluorescent labelled phalloidin (AlexaFluor555-labeled; Life Technologies, Darmstadt, Germany) and secondary antibody (AlexaFluor488-labeled). After washing, the stained samples were imbedded in ProLong® Gold antifade reagent including DAPI (Life Technologies). The following microscopy analysis was performed using a Keyence BZ-9000 fluorescence microscope (Neu-Isenburg, Germany). Additionally, Scanning Electron Microscopy (SEM) was performed to analyse cellular adhesion. Therefore, both cell lines were cultivated on the prepared samples, washed and fixed overnight (2% glutaraldehyde, 0.2 M sodium cacodylate). Afterwards the cells were contrasted with 1% osmium tetroxide in a combination with 1% tannic acid getting a more precise staining of superfine structures.[34] Subsequently cells were dehydrated using rising ethanol concentrations, dried using hexamethyldisilazane (HDMS) and sputtered with gold. The samples were analysed with a FEI ESEM Quanta 400 FEG (FEI, Hillsboro, USA) scanning electron microscope at 10 kV.

### 3.7 Protein analysis using MALDI-TOF/TOF MS/MS

**3.7.1 Cell lysis, protein extraction and quantification.** HUVEC were gently scraped from the surfaces, washed with ice cold PBS and suspended in 2D-DIGE buffer (8 M urea, 2 M thiourea, 4% CHAPS, 30 mM Tris pH 8.5, 1× protease inhibitor cocktail). To lyse the cells 0.5 μm stainless steel beads were used with a bead beater (Next Advance, US). To obtain a soluble protein extract and removing the cell debris, samples were centrifuged at 13 000 × *g* for 10 min at 4 °C. To further clarify the supernatants, the samples were centrifuged at 15 000 × *g* for additional 60 min at 4 °C. Protein concentrations were determined by a modified Lowry assay (BioRad, US) and the samples were stored at −80 °C until use.

**3.7.2 Protein labeling for DIGE.** Protein extracts were prepared in DIGE lysis buffer and labeled with Cy2, Cy3 and Cy5 according to the instructions provided by the supplier (Life Tech, USA). In brief, 50 μg of each protein sample was used for labeling. After adjusting the pH of the extract to 8.5, CyDye DIGE Fluor minimal dyes were put directly to the sample and incubated at 4 °C for 30 min. The reactions were terminated by adding lysine for 10 min.

**3.7.3 Two-dimensional (2D) gel electrophoresis.** Labeled protein samples were loaded onto immobilized pH gradient strips (IPG) (pH 5–8) by passive rehydration. Separations based on isoelectric points were performed by using protean isoelectric focusing cell on 11 cm strips using the following conditions: 20 min at 250 V with rapid ramp, 2 h at 4000 V with slow ramp and 2.5 h for 4000 V with rapid ramp until a total of 14.000 V $h^{-1}$ was reached at 20 °C. After isoelectric focusing, strips were washed with buffer I (6 M urea, 375 mM Tris–HCl pH 8.8, 2% SDS, 20% glycerol, 2% (w/v) DTT) for 30 min and then with buffer II (6 M urea, 375 mM Tris–HCl pH 8.8, 2% SDS, 20% glycerol, 2.5% iodoacetamide (w/v)) for 30 min at RT in the dark and subjected to SDS-PAGE by using TGX precast gels in a Dodeca gel running system (Bio-Rad, USA).

**3.7.4 Image analysis.** Gels were imaged with VersaDoc4000 MP (BioRad, USA) by using Quantity One software (BioRad, USA). PDQuest Advance 2D-analysis software (BioRad, USA) was used for comparative analysis of protein spots. The statistical analysis was performed using the Student's *t*-test ($p < 0.05$ were considered as significant). Gel spots that significantly differed in expression (more than 2-fold) were selected and excised from

preparative gels using ExQuest Spot-cutter (Bio-Rad, USA) for protein identification.

**3.7.5 In-gel tryptic digestion.** The selected protein spots were destained/washed with 40% acetonitrile (ACN)/50 mM ammonium bicarbonate ($NH_4HCO_3$) until the gel pieces become colorless, reduced with 10 mM DTT at 80 °C for 30 min and alkylated with 50 mM iodoacetamide at room temperature for 30 min in the dark. Trypsin digestion was carried out by the addition of 20 μl of trypsin (10 ng $\mu l^{-1}$) in 40 mM $NH_4HCO_3$ solution overnight at 37 °C. After trypsin digestion, the protein peptides were desalted/concentrated with C18 ZipTip pipette tips (Millipore, USA) according to the manufacturer's instructions. The concentrated peptides were eluted with 0.8 μl matrix (10 mg $mL^{-1}$ a-cyano-4-hydroxycinnamic acid prepared in 50% acetonitrile, 0.1% trifluoroacetic acid) and they were directly spotted onto a MALDI sample target plate.

### 3.8 MALDI-TOF/TOF MS/MS and database searching

Proteins peptide mass spectra were obtained using MALDI-TOF/TOF MS/MS (ABI 5800; AB Sciex, US). Prior to analysis, the calibration was carried out with a mixture of des-Arg-bradykinin, angiotensin I, Glu1-fibrinopeptide B, ACTH (1–17), ACTH (18–39). In reflector mode a mass precision of 25 ppm was recorded. The major peaks were chosen for further MS/MS analyses. Obtained MS/MS spectra (in reflector positive mode) were used to identify the proteins and NCBI nr and MASCOT database were employed for identification (a tolerance of 25 ppm was considered for peptide and fragment ion mass). Search parameters were set as follows: allowance of one missed cleavage site; enzyme trypsin; carbamidomethyl (cysteine) and oxidation of Met as fixed modification; protein mass unrestricted; monoisotopic mass values. The mass tolerances were selected as ±25 ppm and ±0.4 Da for peptide mass and fragment mass respectively. The numbers of matching peptide masses as well as the comparison of protein properties (experimental and theoretical) were taken to determine the identified proteins. Ion scores were used (as non-probabilistic basis) to achieve proteome scores. Protein scores with $p < 0.05$ were taken as significant.

## 4. Conclusions

In this study, chemical vapour deposition (CVD) and combined CVD with laser ablation methods were used to synthesize nanostructured and micro-/nanostructured topographical features, respectively, in order to achieve selective growth of endothelial cells over smooth muscle cells *via* topography driven cell response. We successfully demonstrated that novel surface topographies can induce a selective cellular attachment and proliferation for human umbilical vein endothelial cells (HUVEC) while suppressing the growth of human umbilical vein smooth muscle cells (HUVSMC). In general, the selective cell growth of EC is of prime importance for stents and other cardiovascular implants. Surfaces with improved selectivity towards HUVEC *via* topography driven cell response mechanism can potentially help to reduce in-stent restenosis and other postoperative complications caused through excessive migration of SMC onto the stent surface. This topography driven cell selective response concept can be extended to dental and orthopedic implants and even for cell separation and isolation platforms.

## Acknowledgements

This work was supported by the German Federal Ministry of Education and Research (BMBF) and The Scientific and Technological Council of Turkey (TUBITAK) in the context of the Research Project IntenC (contract number: 01DL12034A; 01DL12034B; 110M760). The authors would like to thank Mrs I. Marsollek for her assistance during the cell culture experiments.

## References

1 D. Fiorella, F. C. Albuquerque, V. R. Deshmukh and C. G. McDougall, *Am. J. Neuroradiol.*, 2004, **25**, 1764–1767.
2 B. P. Mwipatayi, S. J. Beningfield, L. E. White, A. Irish, M. Abbas and K. Sieunarine, *Eur. J. Vasc. Endovasc. Surg.*, 2005, **29**, 479–488.
3 A. Colombo, J. Drzewiecki, A. Banning, E. Grube, K. Hauptmann, S. Silber, D. Dudek, S. Fort, F. Schiele, K. Zmudka, G. Guagliumi, M. E. Russell and T. I. S. Grp, *Circulation*, 2003, **108**, 788–794.
4 T. Inoue, K. Croce, T. Morooka, M. Sakuma, K. Node and D. I. Simon, *JACC: Cardiovasc. Inte.*, 2011, **4**, 1057–1066.
5 N. Li, G. Chen, J. Liu, Y. Xia, H. B. Chen, H. Tang, F. M. Zhang and N. Gu, *ACS Appl. Mater. Interfaces*, 2014, **6**, 17134–17143.
6 N. Blanchemain, M. R. Aguilar, F. Chai, M. Jimenez, E. Jean-Baptiste, A. El-Achari, B. Martel, H. F. Hildebrand and J. S. Roman, *Biomed. Mater.*, 2011, **6**, 065003.
7 C. Gonzalez-Garcia, S. R. Sousa, D. Moratal, P. Rico and M. Salmeron-Sanchez, *Colloids Surf., B*, 2010, **77**, 181–190.
8 C. Aktas, E. Dorrschuck, C. Schuh, M. M. Miro, J. Lee, N. Putz, G. Wennemuth, W. Metzger, M. Oberringer, M. Veith and H. Abdul-Khaliq, *Mater. Sci. Eng., C*, 2012, **32**, 1017–1024.
9 C. C. Mohan, P. R. Sreerekha, V. V. Divyarani, S. Nair, K. Chennazhi and D. Menon, *J. Mater. Chem.*, 2012, **22**, 1326–1340.
10 A. F. von Recum and T. G. van Kooten, *J. Biomater. Sci., Polym. Ed.*, 1995, **7**, 181–198.
11 R. G. Flemming, C. J. Murphy, G. A. Abrams, S. L. Goodman and P. F. Nealey, *Biomaterials*, 1999, **20**, 573–588.
12 L. Wang and R. L. Carrier, in *Advances in Biomimetics*, ed. M. Cavrak, 2011, pp. 453–472.
13 M. Ponticos and B. D. Smith, *J. Biomed. Res.*, 2014, **28**, 25–39.
14 M. Oberringer, E. Akman, J. Lee, W. Metzger, C. K. Akkan, E. Kacar, A. Demir, H. Abdul-Khaliq, N. Putz, G. Wennemuth, T. Pohlemann, M. Veith and C. Aktas, *Mater. Sci. Eng., C*, 2013, **33**, 901–908.
15 D. W. Powell, R. C. Mifflin, J. D. Valentich, S. E. Crowe, J. I. Saada and A. B. West, *Am. J. Physiol.-Cell Ph.*, 1999, **277**, C1–C19.

 

16 Y. Y. Wu and P. D. Yang, *J. Am. Chem. Soc.*, 2001, **123**, 3165–3166.
17 M. Veith, O. C. Aktas, W. Metzger, D. Sossong, H. U. Wazir, I. Grobelsek, N. Putz, G. Wennemuth, T. Pohlemann and M. Oberringer, *Biofabrication*, 2010, **2**, 035001.
18 C. K. Akkan, M. E. Hammadeh, A. May, H. W. Park, H. Abdul-Khaliq, T. Strunskus and O. C. Aktas, *Lasers Med. Sci.*, 2014, **29**, 1633–1639.
19 J. D. Humphries, P. Wang, C. Streuli, B. Geiger, M. J. Humphries and C. Ballestrem, *J. Cell Biol.*, 2007, **179**(5), 1043–1057.
20 M. Nikkhah, F. Edalat, S. Manoucheri and A. Khademhosseini, *Biomaterials*, 2012, **33**(21), 5230–5246.
21 M. S. Lord, M. Foss and F. Besenbacher, *Nano Today*, 2010, **5**, 66–78.
22 J. Lee, L. K. Schwarz, C. K. Akkan, M. M. Miro, O. T. Abad, K. H. Schafer, M. Veith and C. Aktas, *Phys. Status Solidi A*, 2013, **210**, 952–956.
23 K. Kiefer, J. Lee, A. Haidar, M. Martinez Miro, C. Kaan Akkan, M. Veith, O. Cenk Aktas and H. Abdul-Khaliq, *Nanotechnology*, 2014, **25**, 495101.
24 T. D. Pollard and G. G. Borisy, *Cell*, 2003, **112**, 453–465.
25 M. Miettinen and J. F. Fetsch, *Hum. Pathol.*, 2000, **31**, 1062–1067.
26 L. Mestroni and M. R. Taylor, *J. Am. Coll. Cardiol.*, 2008, **52**, 1261–1262.
27 Y. Gruenbaum, R. D. Goldman, R. Meyuhas, E. Mills, A. Margalit, A. Fridkin, Y. Dayani, M. Prokocimer and A. Enosh, *Int. Rev. Cytol.*, 2003, **226**, 1–62.
28 J. M. Dave and K. J. Bayless, *Microcirculation*, 2014, **21**, 333–344.
29 J. E. Eriksson, T. He, A. V. Trejo-Skalli, A. S. Harmala-Brasken, J. Hellman, Y. H. Chou and R. D. Goldman, *J. Cell Sci.*, 2004, **117**, 919–932.
30 M. Gonzales, B. Weksler, D. Tsuruta, R. D. Goldman, K. J. Yoon, S. B. Hopkinson, F. W. Flitney and J. C. Jones, *Mol. Biol. Cell*, 2001, **12**, 85–100.
31 F. Orosz, J. Olah and J. Ovadi, *IUBMB Life*, 2006, **58**, 703–715.
32 M. Veith, J. Lee, M. Martinez Miro, C. K. Akkan, C. Dufloux and O. C. Aktas, *Chem. Soc. Rev.*, 2012, **41**, 5117–5130.
33 M. Veith, E. Sow, U. Werner, C. Petersen and O. C. Aktas, *Eur. J. Inorg. Chem.*, 2008, 5181–5184.
34 A. Katsen-Globa, I. Meiser, Y. A. Petrenko, R. V. Ivanov, V. I. Lozinsky, H. Zimmermann and A. Yu. Petrenko, *J. Mater. Sci.: Mater. Med.*, 2014, **25**(3), 857–871.